Article

# Deep, ultra-hot-melting residues as cradles of mantle diamond

https://doi.org/10.1038/s41586-022-05665-2

Received: 29 January 2022

Accepted: 14 December 2022

Published online: 15 March 2023

Check for updates

Carl Walsh[1], Balz S. Kamber[1]✉ & Emma L. Tomlinson[2]

The ancient stable continents are up to 250 km deep, with roots extending into the diamond stability field[1]. These cratons owe their mechanical strength to being cool and rigid[2], features inherited from extensive melt extraction[1,3]. The most prominent model for craton formation anticipates dominant melting at relatively shallow depth (50–100 km) above diamond stability[4–7], followed by later imbrication to form the deeper roots[8,9]. Here we present results from thermodynamic and geochemical modelling of melting at sufficiently high temperatures to produce the very magnesian olivine of cratonic roots[10]. The new closed-system and open-system modelling reproduces the observed cratonic mantle mineral compositions by deep (about 200 km) and very hot melting (≥1,800 °C), obviating the need for shallow melting and stacking. The modelled highly magnesian liquids (komatiites) evolve to Al-enriched and Ti-depleted forms, as observed in the greenstone belts at the fossil surface of cratons[11]. The paucity of Ti-depleted komatiite[12] implies that advanced closed-system isochemical melting (>1,825 °C) was much less common than open-system interaction between deeper liquids and melting of existing refractory mantle. The highly refractory compositions of diamond inclusion minerals could imply preferential diamond growth in the more reducing parts of the cratonic root, depleted by ultra-hot melting in response to heat plumes from a deeper former boundary layer that vanished at the end of the Archaean[13].

Diamonds dominantly originate in the deep mantle roots of Archaean cratons, which differ from younger continental lithosphere. The Archaean cratonic roots experienced extensive melt depletion, expressed in the high to very high forsterite content (Fo = 100 × MgO/(FeO + MgO)) of olivine from mantle xenoliths (Fo91–Fo94), contrasting with olivine from off-craton and other young mantle peridotite (Fo89–Fo91)[14,15]. On the surface of cratons, belts of supracrustal rocks host the Earth's hottest known lavas (komatiites), whose diverse origins reflect advanced, very-high-temperature melting over a range of depths[11,12]. The original geological models for such melting were based on high-pressure experiments and imagined a variety of formation processes at very high temperatures at the great depth at which diamonds and garnet-bearing cratonic peridotites reside[3,10,16,17].

These ideas have given way to the favoured model at present of shallow melting and later stacking or inversion of residual lithosphere into cratonic roots deep enough to extend into the diamond stability field. This was proposed to explain two new pieces of mineralogical and geochemical evidence. First, it transpired that garnets from deep cratonic mantle roots can be very Cr-rich (Extended Data Fig. 1a), particularly those found as inclusions in diamond (DI). Interpretation of thermodynamic phase diagrams suggested that it is difficult and unlikely to make Cr-rich garnet at depths corresponding to pressures >2.5–3.0 GPa (ref. [4]). Instead, melting was predicted to have occurred at shallow depth, producing residues with high Cr/Al-containing spinel, which later converted to garnet on deepening of the cratonic root[5,6,8]. Second, deep, garnet-bearing cratonic mantle rocks were found to have low concentrations of heavy rare earth elements (HREEs). Geochemical modelling suggested that the presence of residual garnet with high HREE partition coefficients ($D$) would retain HREEs during melting[7,18]. By contrast, the shallower mantle Al-phase spinel has low $D_{REE}$, resulting in residual peridotites depleted in HREEs. Again, later conversion into garnet peridotite is predicted by means of thickening originally shallow spinel-facies lithospheric mantle. A notable limitation of the present thinking is that, even at a hotter potential temperature of about 1,600 °C, advanced relatively shallow melting cannot produce olivine with Fo > 93 found in many DIs[19] and xenoliths (Extended Data Fig. 1b).

## Melt extraction modelling

We used a thermodynamic model to explore refractory peridotite and liquid phase relationships at much higher temperatures than before, aided by improved liquid models, inclusion of $Cr_2O_3$ as a system component and revised activity models for pyroxenes[20,21]. Modelling now allows us to investigate the experimentally poorly known refractory space in greater detail than previously possible. Outputs of three model arrangements were explored: a physically implausible fertile[22] single-batch model retaining unrealistically high fractions of liquid[23]; an isochemical incremental model generating depleted compositions through repeated extractions of melt from an originally fertile source; and an open-system model in which refractory solid

[1]School of Earth and Atmospheric Sciences, Queensland University of Technology, Brisbane, Queensland, Australia. [2]Geology, School of Natural Sciences, Trinity College Dublin, Dublin, Ireland. ✉e-mail: balz.kamber@qut.edu.au

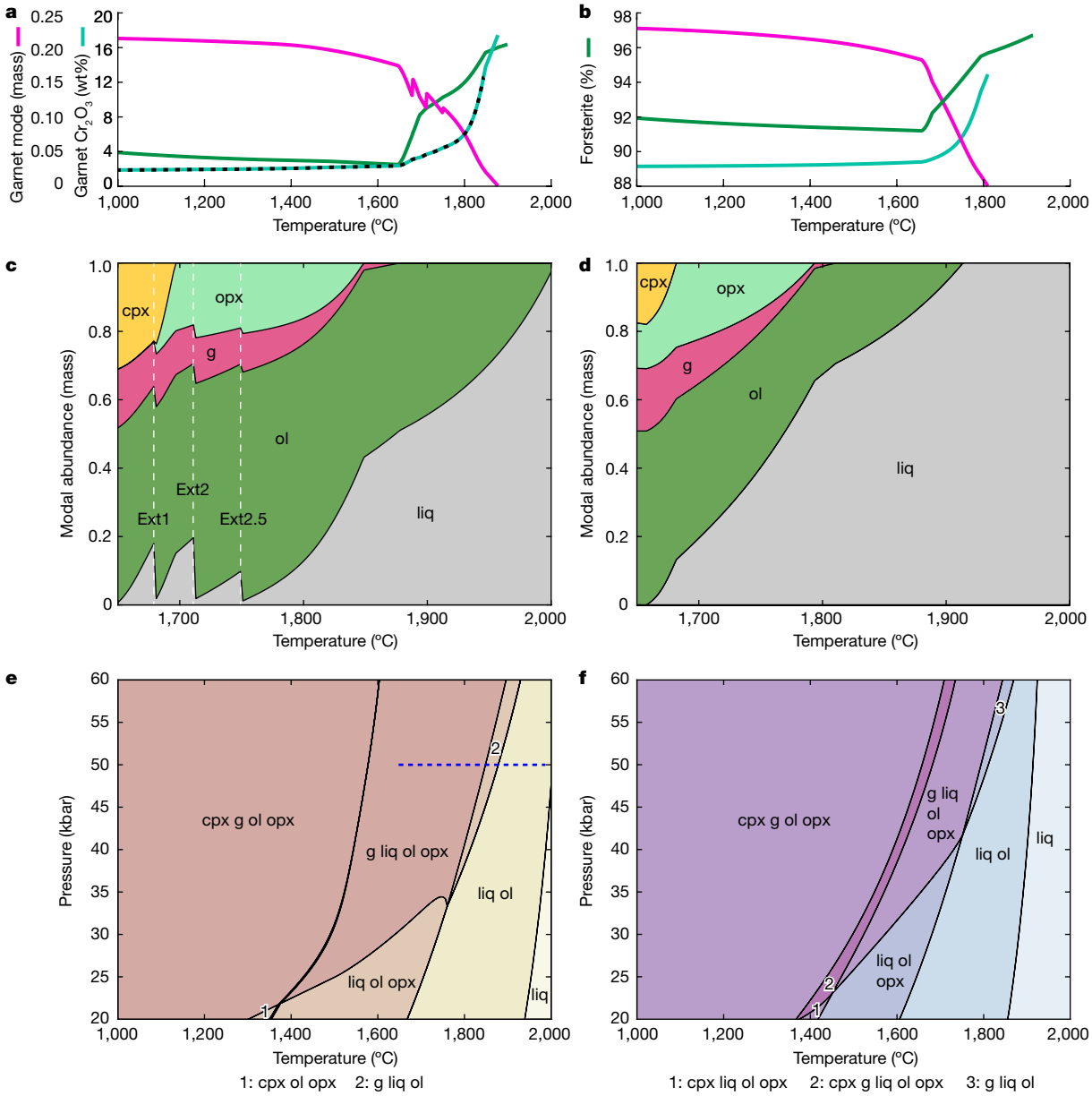


**Fig. 1 | Stability fields, abundances and selected chemical attributes of modelled mantle minerals.** Comparison of results from incremental (left) versus open-system modelling (right). The panels in the top row compare garnet mode in residue (pink), garnet $Cr_2O_3$ content (teal; black dashed overlay with spinel) and olivine forsterite (green) with temperature at 5 GPa (**a** and **b**). The middle panels (**c** and **d**) show modal abundances of phases, with clear persistence of garnet and orthopyroxene stability to very high temperatures. The bottom row compares pressure–temperature phase stability fields in refractory (**e**, after Ext2.5 from KR4003) versus open-system (hybrid #1) space (**f**), with dashed lines indicating the mode box position.

residues were hybridized[24] with liquids from greater depths (see Methods). In the incremental model, starting from fertile mantle (KR4003 (ref. [22])), across three melt extractions (Fig. 1a,c,e), the residue rapidly becomes more refractory, evolving from pyrolite to harzburgite and garnet dunite with loss of incompatible $TiO_2$, $Al_2O_3$, $Fe_2O_3$, CaO, $Na_2O$, $K_2O$ and (more modestly) FeO, retention of $Cr_2O_3$ and MgO, and little changed $SiO_2$ (Extended Data Table 1). Notably, unlike in the unrealistic single-batch model, in which garnet disappears after modest melt extraction between 2.5 and 4.0 GPa (ref. [4]) (Extended Data Fig. 2), it remains the second-to-last phase on the liquidus above 3.3 GPa in the refractory system.

The first new key finding relates to the high $Cr_2O_3$ in garnet (Supplementary Data 1). Even in the single-batch model, garnet at 5 GPa can reach $Cr_2O_3$ concentrations as high as 10–11 wt% close to garnet exhaustion (Supplementary Data 2), with no need for a high Cr/Al precursor rock. In the incremental melting model, garnet persists to 1,877 °C at 5 GPa, reducing in abundance from 15% by mass on the solidus to less than 3% at orthopyroxene-out (Fig. 1a). Together with the decrease in garnet mode, its $Cr_2O_3$ concentration increases very strongly from 4 to 18 wt% (Fig. 1a). Regardless of pressure, it is found that only the last remaining garnet in the system, within 30 °C of the garnet-out reaction, is very Cr-rich (approximately 6–18 wt% $Cr_2O_3$), similar to the G10-type chemical signature classically used for diamond prospectivity[25]. This upper value is very close to the maximum $Cr_2O_3$ observed in garnet DIs (Extended Data Fig. 1a).

## Open-system deep mantle melting

Melting at the very high temperatures of the incremental model is geologically most plausible when heat transfer from even deeper

liquids originating below the lithosphere is considered. This open system was simulated with hybridization[24] of deep (7 GPa for hybrids #1 and #3; 8 GPa for #2) komatiites with variably refractory resident lithosphere (Extended Data Fig. 3; see Methods for details). The less refractory hybrids #1 and #2 (results of #1 shown in Fig. 1b,d,f) reach maximum $Cr_2O_3$ in garnet of 12.9 wt% (Fig. 1b and Supplementary Data 3) and 13.8 wt%, respectively. Only the hybrid (#3) of an already highly refractory lithosphere with the lowest addition (20% by mass) of deep komatiite produces Cr concentrations in garnet of 15.0 wt% (Supplementary Data 4), which is still not as high as in the incremental model. Owing to chromite spinel occurring as DIs[26], the possibility of spinel existing at very high pressures was also explored (Extended Data Fig. 5). This modelling indicated that spinel would replace garnet as the second-to-last phase on the liquidus. We deem this finding unrealistic by comparison with experiments[22] (see also Methods) and because the model spinel composition is far lower in Cr than that observed in DIs[26].

All models yield highly magnesian olivine in residues (Extended Data Fig. 4). In the incremental model, increase in Fo content with increasing temperature is slowest, owing to persistence of orthopyroxene (Fig. 1c), which competes for MgO. In the single-batch and hybrid models, Fo content increases more rapidly, therefore, the incremental model predicts very Cr-rich garnet to coexist with the least extreme olivine (about 0.5 Fo units lower than in fertile and hybrid residues), more similar to olivine DIs[26] (Extended Data Fig. 1b).

## Modelling HREE loss

Dynamic incongruent melting modelling was used to calculate HREE systematics of residues after incremental melt extractions. The melting pathway was based on the outputs of the proportions and compositions of all phases across the pseudosections[20], which yielded exact stoichiometries for melting reactions. A series of isobaric trajectories (4.0, 5.0 and 5.5 GPa) were modelled to test deep in situ lithospheric melting as an alternative to the traditional deep melting hypothesis of polybaric fractional melting. Starting from the solidus, the relative consumption (and crystallization) rates of solids were calculated until a phase boundary or a critical melt fraction was encountered, whichever was earlier. Six melting reactions occur from the solidus until garnet-out (Fig. 2 inset). For each melting reaction, appropriate individual partition coefficients were calculated for all phases from their compositions and equilibrium conditions (Extended Data Table 2 and Methods) as inputs for the incongruent dynamic trace element model[27] (Supplementary Data 5). In one version, a small fraction of liquid was retained at extraction and the other retained no liquid. Regardless, the resulting concentration trajectories in lutetium (Lu) versus ytterbium (Yb) space are very similar (Fig. 2), with minimal difference between the 4.0-GPa, 5.0-GPa and 5.5-GPa models, all producing a marked Lu and Yb loss. This shows that HREE depletion also occurs by high-pressure melting in the presence of garnet. It can be attributed to near-complete consumption of garnet, early consumption of clinopyroxene, steady formation of peritectic orthopyroxene and repeated extraction of liquid.

Our results differ substantially from earlier studies[7] that did not model incremental loss of liquid, did not account for changing melt reaction stoichiometries and used generic garnet $D_{REE}$ (ref. [18]) calibrated for much lower pressure mid-ocean-ridge melting (see Extended Data Fig. 6). Lu and Yb concentrations in natural harzburgites plot along our model trajectories corresponding to residues between liquid extraction increment 2 and orthopyroxene-out in our model. This corresponds to 35–65 wt% cumulative melt extraction at 5 GPa and yields garnet Cr concentrations that match those observed in the xenoliths (Extended Data Fig. 1a,c). When major element outputs from the thermodynamic model are combined with the HREE results, the resulting model residues for the isobaric 5-GPa incremental model reproduce empirical garnet harzburgite data very well in Mg/Al versus Yb space (Extended Data Fig. 7). Limitations of the pyroxene activity–composition models

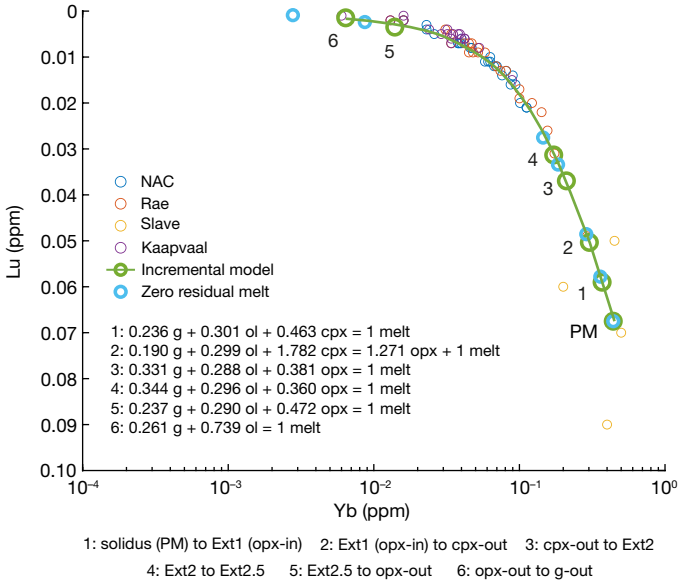


**Fig. 2 | Modelled loss of HREEs during progressive melt extraction from deep mantle.** Comparison of HREE systematics in observed garnet harzburgites from four cratons with residues after incremental incongruent melt extraction (xenolith data[7] $n = 70$, colour-coded by craton). Residue compositions were calculated as six incremental melt extraction steps and the incongruent melting stoichiometries are listed. The effect of modest liquid in the residue during extraction can be seen between the incremental model and $\varphi = 0$, in which no melt is retained. NAC, North Atlantic Craton; PM, primitive mantle.

(>6 GPa) preclude testing the open-system models for HREEs, as liquids are derived from greater depths—environments with poorly constrained $D_{REE}$ at present.

## Highly refractory diamond cradles

Our results show that the two pieces of evidence previously used to strongly argue against inherently deep in situ formation of cratonic garnet harzburgite are no longer unambiguous. With respect to the extent of Cr enrichment, the key is the expansion of the garnet stability field at 5 GPa in the refractory and open-system models (Fig. 1) compared with the fertile model. Not only is garnet stabilized to much greater temperature (from 1,779 °C to 1,877 °C at 5 GPa), it also becomes much richer in Cr (from a maximum of 11 to 18 wt% $Cr_2O_3$). The natural garnet DIs highest in Cr therefore seem to have formed by means of incremental or open-system melting involving highly refractory lithosphere, leaving behind residues of very depleted harzburgites or even garnet dunites[28]. Most diamondiferous peridotites apparently disaggregated[26] on transport in kimberlite but refractory indicator minerals are commonly found alongside diamond in concentrates and the few diamondiferous xenoliths that survived to surface are extremely refractory garnet harzburgite and dunite[29], implying that diamond preferentially formed in those environments.

The tendency for DI garnet and olivine to be more Cr-rich and Mg-rich, respectively, than in harzburgite xenoliths has two most obvious explanations. First, DIs could be vestiges of an overall highly refractory original lithosphere that was later refertilized and sampled by xenoliths. Second, the original ancient lithospheric mantle was variably depleted, with diamond mainly forming in the most refractory, possibly subordinate, portions. Owing to the representativeness of cratonic mantle samples, it is not feasible to conclusively evaluate the two possibilities with them alone. Our new perspective is that the chemistry of komatiites affords independent insight into the extent of cratonic mantle depletion in the Archaean. Komatiites are classified into Al-depleted (ADK),

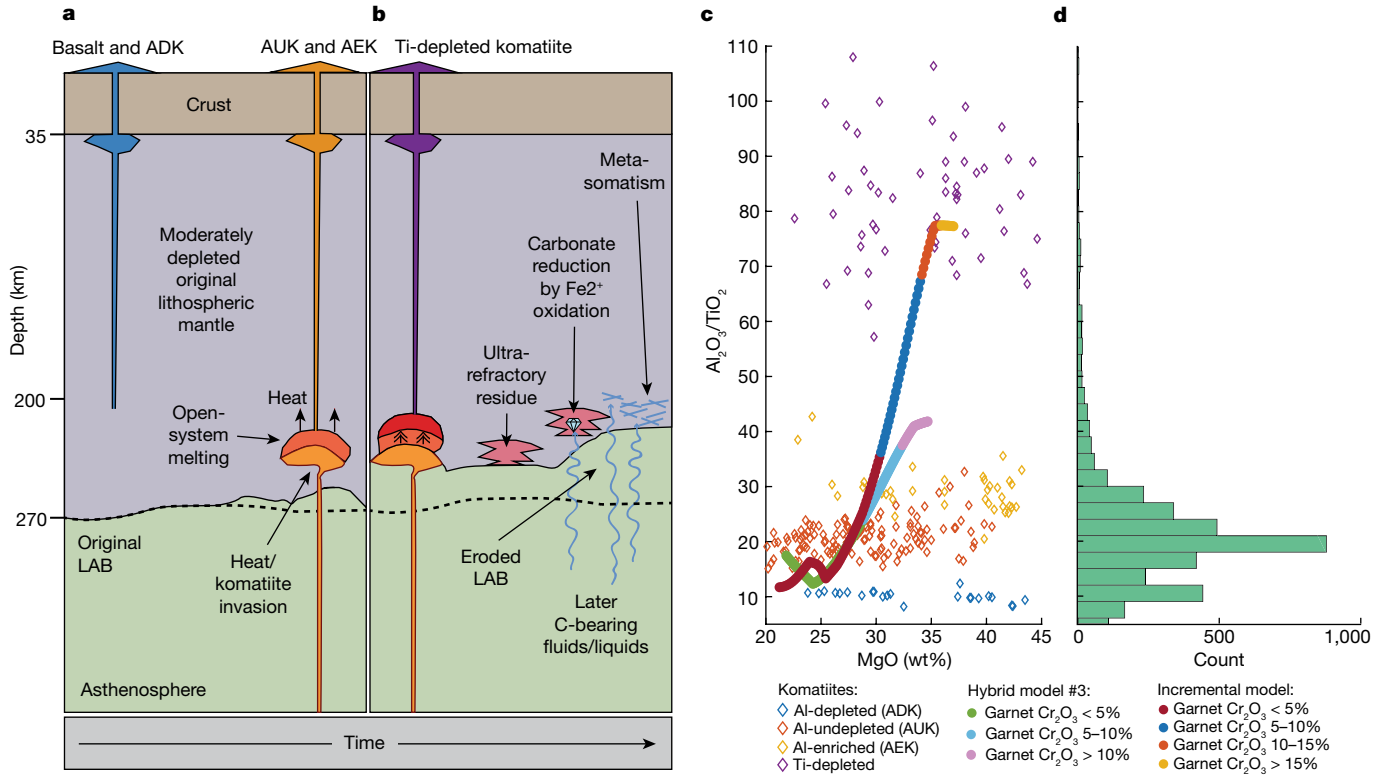


**Fig. 3 | Geodynamic model explaining the evolution of deep cratonic mantle, related volcanic rock chemistry and formation of diamond cradles. a**, Evolution of cratonic lithosphere, beginning with formation of moderately depleted but thick (lithosphere–asthenosphere boundary (LAB) ≫200 km) protolithosphere to yield basalt and ADK. **b**, Archaean channelized heat upwellings and sublithospheric komatiites locally remelted the protolithosphere. This generated AUK and AEK and caused further incremental isochemical melting, leaving behind highly refractory residues accounting for 8–28% of the deep craton root. Subsequent invasion of volatile-rich fluids metasomatized and generally oxidized the deepest lithosphere over time but in ultra-refractory residues formed diamond. **c**, Evolution of modelled liquids in MgO versus $Al_2O_3/TiO_2$ compared with classic komatiites[11,30,40], $n = 257$. Melting models colour-coded for garnet Cr concentration. **d**, Histogram of $Al_2O_3/TiO_2$ of 3,829 komatiites.

Al-undepleted (AUK) and Al-enriched (AEK) based on the $Al_2O_3/TiO_2$ ratio. This is not due to fractional crystallization, as $Al_2O_3/TiO_2$ is not substantially correlated with MgO (Fig. 3c).The hottest komatiite is rare, very Ti-depleted[12] AEK known from several cratons[15]. Komatiites were emplaced in this order of classification on some cratons (for example, Kaapvaal[11]), whereas on others, they exist in close stratigraphic proximity (for example, Abitibi[30]). Our incremental 5-GPa model produces liquids with increasing $Al_2O_3/TiO_2$ (Fig. 3c), eventually reaching $Al_2O_3/TiO_2 > 70$ (Fig. 3c), whereas only in the most refractory hybrid model (#3) liquids reach $Al_2O_3/TiO_2$ of about 40. Because the model outputs the chemistries of residual phases (that is, $Cr_2O_3$ in garnet) as well as those of the coexisting liquids (that is, $Al_2O_3/TiO_2$), it is possible to use the global Archaean komatiite database (Fig. 3d) to estimate how common refractory, potentially diamond-bearing residues could have been. In the incremental model, residues with >5 wt% $Cr_2O_3$ garnets (representing 87% of all DI garnets) require liquids with $Al_2O_3/TiO_2 > 36.3$. Only 7.6% of global komatiites meet this criterion. Hybrid model #3 requires liquids with $Al_2O_3/TiO_2 > 23.7$ for >5 wt% $Cr_2O_3$ garnets, which would satisfy 28.4% of the observed komatiites. If the predominant mode of deep cratonic mantle melting was incremental, then highly refractory cratonic peridotite was always subordinate (7.6%). In the more probable case of open-system melting, komatiite chemistry suggests that up to about 28% of the deep mantle could originally have been sufficiently refractory to stabilize highly chromian garnet. Regardless, only incremental melting (for example, at 5 GPa and 1,827 °C) can generate Ti-depleted komatiite liquid very close in composition (Extended Data Fig. 8) to the archetype from Commondale[12]. It may be notable that this komatiite carried Al-rich olivine crystals from >250 km depth to the surface, providing a direct link to very deep melting[31].

## Geodynamic implications of deep melting

In our preferred model, original mantle lithosphere was deep and moderately depleted (Fig. 3a). Episodic heat upwellings[13] and arrival of deeper-sourced liquids[32], possibly from a now-vanished thermal boundary layer in the mantle transition zone, caused further local open-system melting, yielding AUK and AEK. This was accompanied by further incremental melting, erupting very high $Al_2O_3/TiO_2$ komatiite. The modified deep Archaean cratonic mantle was thus variably depleted, with highly refractory residues making up 8–28% of its volume (Fig. 3b). Because ferric iron ($Fe^{3+}$) is incompatible[33], the most refractory residues ended up with the lowest $Fe^{3+}/Fe^{2+}$ ratios[34]. It is reasonable to suggest that these residues had the highest potential to reduce carbon from invading carbonate fluids[35] to diamond. The prominent peak in DI encapsulation at 190–210 km (ref. [36]) suggests particularly effective carbonate reduction at that depth (Fig. 3b). Depth distribution, radiometric dating of metasomatism[37] and fossil ancient geotherms[38] suggest that, over time, the originally deeper lithosphere base was weakened (Fig. 3b) and removed. The key feature of Archaean mantle was episodic but localized very hot upwelling of heat and melt, such as in heat pipes[39], conditions that primed portions of cratonic mantle as 'cradles of diamond' formation and caused eruption of the Earth's hottest known lavas.

## Online content

Any methods, additional references, Nature Portfolio reporting summaries, source data, extended data, supplementary information, acknowledgements, peer review information; details of author contributions

and competing interests; and statements of data and code availability are available at https://doi.org/10.1038/s41586-022-05665-2.


1. Kopylova, M. G. & Caro, G. Mantle xenoliths from the southeastern Slave craton: evidence for chemical zonation in a thick, cold lithosphere. *J. Petrol.* **45**, 1045–1067 (2004).
2. Begg, G. C. et al. The lithospheric architecture of Africa: seismic tomography, mantle petrology, and tectonic evolution. *Geosphere* **5**, 23–50 (2009).
3. Griffin, W. et al. The origin and evolution of Archean lithospheric mantle. *Precambrian Res.* **127**, 19–41 (2003).
4. Canil, D. Mildly incompatible elements in peridotites and the origins of mantle lithosphere. *Lithos* **77**, 375–393 (2004).
5. Brey, G. P. & Shu, Q. The birth, growth and ageing of the Kaapvaal subcratonic mantle. *Mineral. Petrol.* **112**, 23–41 (2018).
6. Pearson, D. G. et al. Deep continental roots and cratons. *Nature* **596**, 199–210 (2021).
7. Wittig, N. et al. Origin of cratonic lithospheric mantle roots: a geochemical study of peridotites from the North Atlantic Craton, West Greenland. *Earth Planet. Sci. Lett.* **274**, 24–33 (2008).
8. Stachel, T., Viljoen, K. S., Brey, G. & Harris, J. W. Metasomatic processes in lherzolitic and harzburgitic domains of diamondiferous lithospheric mantle: REE in garnets from xenoliths and inclusions in diamonds. *Earth Planet. Sci. Lett.* **159**, 1–12 (1998).
9. Lee, C.-T. A. & Chin, E. J. Calculating melting temperatures and pressures of peridotite protoliths: implications for the origin of cratonic mantle. *Earth Planet. Sci. Lett.* **403**, 273–286 (2014).
10. Boyd, F. R. Compositional distinction between oceanic and cratonic lithosphere. *Earth Planet. Sci. Lett.* **96**, 15–26 (1989).
11. Robin-Popieul, C. C. et al. A new model for Barberton komatiites: deep critical melting with high melt retention. *J. Petrol.* **53**, 2191–2229 (2012).
12. Wilson, A. H. The late-Paleoarchean ultra-depleted Commondale komatiites: Earth's hottest lavas and consequences for eruption. *J. Petrol.* **60**, 1575–1620 (2019).
13. Davies, G. F. Episodic layering of the early mantle by the 'basalt barrier' mechanism. *Earth Planet. Sci. Lett.* **275**, 382–392 (2008).
14. Pearson, D. G. & Wittig, N. Formation of Archaean continental lithosphere and its diamonds: the root of the problem. *J. Geol. Soc.* **165**, 895–914 (2008).
15. Kamber, B. S. & Tomlinson, E. L. Petrological, mineralogical and geochemical peculiarities of Archaean cratons. *Chem. Geol.* **511**, 123–151 (2019).
16. Takahashi, E. & Scarfe, C. M. Melting of peridotite to 14 GPa and the genesis of komatiite. *Nature* **315**, 566–568 (1985).
17. Herzberg, C. Depth and degree of melting of komatiites. *J. Geophys. Res. Solid Earth* **97**, 4521–4540 (1992).
18. Simon, N. S. C., Carlson, R. W., Pearson, D. G. & Davies, G. R. The origin and evolution of the Kaapvaal cratonic lithospheric mantle. *J. Petrol.* **48**, 589–625 (2007).
19. Schulze, D. J. A classification scheme for mantle-derived garnets in kimberlite: a tool for investigating the mantle and exploring for diamonds. *Lithos* **71**, 195–213 (2003).
20. Holland, T. J. B., Green, E. C. R. & Powell, R. Melting of peridotites through to granites: a simple thermodynamic model in the system KNCFMASHTOCr. *J. Petrol.* **59**, 881–900 (2018).
21. Tomlinson, E. L. & Holland, T. J. A thermodynamic model for the subsolidus evolution and melting of peridotite. *J. Petrol.* **62**, egab012 (2021).
22. Walter, M. J. Melting of garnet peridotite and the origin of komatiite and depleted lithosphere. *J. Petrol.* **39**, 29–60 (1998).
23. Schmeling, H. & Arndt, N. Modelling komatiitic melt accumulation and segregation in the transition zone. *Earth Planet. Sci. Lett.* **472**, 95–106 (2017).
24. Tomlinson, E. L. & Kamber, B. S. Depth-dependent peridotite-melt interaction and the origin of variable silica in the cratonic mantle. *Nat. Commun.* **12**, 1082 (2021).
25. Grütter, H. S., Gurney, J. J., Menzies, A. H. & Winter, F. An updated classification scheme for mantle-derived garnet, for use by diamond explorers. *Lithos* **77**, 841–857 (2004).
26. Stachel, T. & Harris, J. The origin of cratonic diamonds—constraints from mineral inclusions. *Ore Geol. Rev.* **34**, 5–32 (2008).
27. Zou, H. & Reid, M. R. Quantitative modeling of trace element fractionation during incongruent dynamic melting. *Geochim. Cosmochim. Acta* **65**, 153–162 (2001).
28. Pokhilenko, N. P., Pearson, D. G., Boyd, F. R. & Sobolev, N. V. Megacrystalline dunites and peridotites: hosts for Siberian diamonds. *Ann. Rep. Dir. Geophys. Lab.* 11–18 (1991).
29. Viljoen, K., Swash, P., Otter, M., Schulze, D. & Lawless, P. Diamondiferous garnet harzburgites from the Finsch kimberlite, Northern Cape, South Africa. *Contrib. Mineral. Petrol.* **110**, 133–138 (1992).
30. Sproule, R. A., Lesher, C. M., Ayer, J. A., Thurston, P. C. & Herzberg, C. T. Spatial and temporal variations in the geochemistry of komatiites and komatiitic basalts in the Abitibi greenstone belt. *Precambrian Res.* **115**, 153–186 (2002).
31. Wilson, A. & Bolhar, R. Olivine in komatiite records origin and travel from the deep upper mantle. *Geology* **50**, 351–355 (2021).
32. McKenzie, D. Speculations on the generation and movement of komatiites. *J. Petrol.* **61**, egaa061 (2020).
33. Canil, D. & O'Neill, H. S. C. Distribution of ferric iron in some upper-mantle assemblages. *J. Petrol.* **37**, 609–635 (1996).
34. McCammon, C. & Kopylova, M. A redox profile of the Slave mantle and oxygen fugacity control in the cratonic mantle. *Contrib. Mineral. Petrol.* **148**, 55–68 (2004).
35. McCammon, C., Griffin, W. L., Shee, S. & O'Neill, H. S. C. Oxidation during metasomatism in ultramafic xenoliths from the Wesselton kimberlite, South Africa: implications for the survival of diamond. *Contrib. Mineral. Petrol.* **141**, 287 (2001).
36. Nimis, P., Preston, R., Perritt, S. H. & Chinn, I. L. Diamond's depth distribution systematics. *Lithos* **376–377**, 105729 (2020).
37. Shu, Q. & Brey, G. P. Ancient mantle metasomatism recorded in subcalcic garnet xenocrysts: temporal links between mantle metasomatism, diamond growth and crustal tectonomagmatism. *Earth Planet. Sci. Lett.* **418**, 27–39 (2015).
38. Hoare, B. C., Tomlinson, E. L. & Kamber, B. S. Evidence for a very thick Kaapvaal craton root: implications for equilibrium fossil geotherms in the early continental lithosphere. *Earth Planet. Sci. Lett.* **597**, 117796 (2022).
39. Moore, W. B. & Webb, A. A. G. Heat-pipe earth. *Nature* **501**, 501–505 (2013).
40. Nesbitt, R., Sun, S.-S. & Purvis, A. Komatiites; geochemistry and genesis. *Can. Mineral.* **17**, 165–186 (1979).

# Methods

### Major element starting composition and THERMOCALC modelling

We selected KR4003 (ref. [22]) (Extended Data Table 1), a pyrolitic garnet peridotite, as the broadly undepleted starting composition because its phase relationships, compositions and melting products are very well constrained by empirical and experimental data. In our model, it represents the primitive, fertile mantle. Melting of KR4003 was investigated from 2–6 GPa, 1,000–2,000 °C (sub-solidus to liquidus).

Major element modelling was conducted in THERMOCALC (https://hpxeosandthermocalc.org/the-thermocalc-software/), an equilibrium thermodynamic modelling program using tc350beta (ref. [41]), dataset tc-ds634 and axfile tc-KNCFMASTOCr (ref. [21]). THERMOCALC produces the most stable phase assemblage from a list of allowed phases by minimizing the Gibbs free energy of a chemical system. In our case, KNCFMASTOCr ($K_2O$–$Na_2O$–CaO–FeO–MgO–$Al_2O_3$–$SiO_2$–$TiO_2$–$Fe_2O_3$–$Cr_2O_3$) for discrete pressure, temperature and chemical (P–T–X) conditions. Our allowed phases were olivine (ol), garnet (g), orthopyroxene (opx), clinopyroxene (cpx), spinel (spn) and melt (liq). The main outputs of THERMOCALC are pressure–temperature phase diagrams of discrete compositions, referred to as pseudosections. THERMOCALC inputs and outputs data in molecular units but for the tables and figures, all outputs have been converted to mass units (for example, weight percent). We operated THERMOCALC by means of a front-end Python program pypsbuilder (https://pypsbuilder.readthedocs.io/en/latest/index.html) in development version[42], compatible with tc350beta, to build, visualize and process pseudosections. pypsbuilder contains post-processing methods in psexplorers that we used to calculate compositional grids over each pseudosection (Extended Data Figs. 2–4) with 1–2 °C temperature spacing.

### Batch and incremental isochemical model details

We considered two isochemical models. First, a single-batch closed system that examined KR4003 from 1,000 °C to liquidus at 5 GPa. This used the (deliberately geologically unrealistic) approach of producing only one batch of melt, mimicking an experimental setup, keeping all melt in equilibrium with the residual phases. In the partially open incremental model, we iteratively extracted three melts from the system at 5 GPa. Extractions 1 and 2 (Ext1 and Ext2, respectively), were driven to 18.5 mol% melt, of which 16.67% was extracted from the system, retaining 10% of the melt in the residue. A final extraction of 8.6% melt (Ext2.5) with 0.8% residual melt was found to deplete the remaining system sufficiently to approximate phases in the most depleted natural harzburgites and diamond inclusions. After each extraction, the residue composition (remaining mineral phases + residual melt) was set as the new bulk composition, as has previously been successfully used in sequential melt extraction from metabasalts[43–45]. Ext1 was taken at 1,680 °C, Ext2 at 1,712 °C and Ext2.5 at 1,750 °C. The resulting incremental model is thus a composite of KR4003 (1,000–1,680 °C), Ext1 (1,680–1,712 °C), Ext2 (1,712–1,750 °C) and Ext2.5 (1,750–2,000 °C). The effect of leaving a small fraction of residual melt in the incremental model is to retain some incompatible elements in the residue that would otherwise become too highly depleted.

### Open-system models

An alternative (or parallel) method to retain incompatible elements is a two-way open system, whereby an incoming liquid reacts with a harzburgite in a fashion akin to assimilation–fractional crystallization to produce a modified harzburgite and a modified liquid. We explored this by modelling hybrid compositions of deeply sourced AUK liquid and residual harzburgite solids following a recently demonstrated model for peridotite-melt interaction[24] reproducing the high orthopyroxene modal abundance found in many cratonic harzburgites. Hybrid #1 is composed of a 1:2 (by mass) mixture of experimental komatiite liquid from run 70.08 at 7 GPa and 1,850 °C (ref. [22]) and a refractory peridotite solid represented by the Ext2 harzburgitic composition. Hybrid #2 is a 1:2 mixture of the liquid from experimental run 78 at 8 GPa and 1,900 °C (ref. [46]) and refractory harzburgite solid Ext2. Hybrid #3 is a 1:4 mixture of the liquid from run 70.08 (ref. [22]) with the more refractory Ext2.5 residue solid composition. All compositions are given in Extended Data Table 1. THERMOCALC pseudosections for each hybrid are shown in Extended Data Fig. 3 and detailed phase compositions were examined at 5 GPa from 1,000 °C to liquidus.

### Model rationale, further parameters and model limitations

We chose to model the effect of deep melt extraction in THERMOCALC because, with the latest dataset and activity-composition models, it has been shown to not only reproduce the positions of most phase boundaries but also the composition of phases from high-pressure experimental constraints[21]. Sequential extractions were modelled at 5 GPa to simulate in situ formation of deep lithosphere within the diamond stability window. The exsolution of garnet from orthopyroxene found in prominent high-silica harzburgites suggests that orthopyroxene originally formed at 5–6 GPa and garnet exsolved during cooling and slight decompression (around 1 GPa) onto the cratonic geotherm[47]. Non-touching garnet and orthopyroxene diamond inclusions suggest prominent entrapment between 5 and 7 GPa (refs. [26,36]). THERMOCALC's activity-composition models are considered robust and accurate to 6 GPa. However, the present orthopyroxene model becomes less stable ≥5 GPa (ref. [21]) and, for this reason, 5-GPa extractions were preferred for this work.

The biggest limitation of the present axfile/dataset concerns spinel. Whereas thermodynamic modelling with the present spinel solution model correctly predicts the pressure of the spinel–garnet boundary at sub-solidus conditions (Extended Data Fig. 2a), it also predicts the existence of a very Mg-rich chromite (spinel) above the liquidus up to 5 GPa. In the relevant experiments[22], such spinel is absent and at >3 GPa, the only Al phase above the solidus is garnet. We regard this discrepancy as an artefact of the present spinel solution model (see more detail below) and, for the incremental and hybridized models after KR4003, spinel was disabled from the possible pseudosection phases.

Because chromite does exist as a diamond inclusion, we nonetheless replicated the incremental model with spinel enabled (Extended Data Fig. 5) to gain potential further insight. In these more refractory compositions than KR4003, in which Mg and Cr are already enriched, THERMOCALC predicts the presence of spinel to even higher pressures of up to 7 GPa, albeit at very low modal abundance (<0.007 at 5 GPa). However, the compositions of these modelled spinels are substantially poorer in $Cr_2O_3$, and richer in $Al_2O_3$ compared with natural diamond inclusion Mg chromites[26]. In the previous spinel activity-composition model[48], the eight spinel group end members mix ideally, without disorder, which is an oversimplification. In the activity-composition model applied here[21], improvements were made to the interaction energies between Mg-Cr spinel and the other spinel end members to fit experiments in the MASCr and CMASCr chemical systems[49]. However, the absence of a Fe-Cr end member remains a limitation.

Because the modelled spinel (when allowed to exist at very high P) replaces garnet as the last phase stable with olivine and liquid at 5 GPa, this also limited the maximum $Cr_2O_3$ content in garnet to 13 wt%. When the high-P spinel is enabled, the model cannot produce the most chromian garnets found in diamond inclusions, regardless of how high the Cr/Al ratio of the system is. Very-high-Cr garnet only forms in spinel-free and orthopyroxene-free garnet harzburgites and dunites.

A further limitation of THERMOCALC is that it does not at present feature mixing models for all elements in each phase. In the present axfile/dataset, K can only be partitioned between clinopyroxene and the liquid, olivine cannot accommodate Al and Cr, and $Fe^{3+}$ is treated as an incompatible element indirectly by means of O. The treatment of Fe speciation in the present model means that, even after moderate liquid

extraction, the bulk $Fe^{3+}/Fe^{2+}$ of the residual harzburgite is very low and does not diminish greatly with further liquid extraction. Although the model trend is qualitatively correct in showing lower $Fe^{3+}/Fe^{2+}$ with increasing degree of melt extraction (as olivine cannot accommodate $Fe^{3+}$ and increases in residue modal abundance[33]), we do not consider the model output $Fe^{3+}/Fe^{2+}$ as an accurate estimate of residue $fO_2$.

### Trace element modelling

The trace element composition of our fertile peridotite was approximated with pyrolite/primitive mantle[50]. The isobaric melting path defined at 5 GPa in our major element incremental model consists of six intervals of distinct melting stoichiometry (Fig. 2 inset). Melting coefficients for each phase were calculated from the slope of a linear model of melt proportion 'versus' phase proportion over individual melting intervals[51].

The REE partition coefficients were calculated for garnet, olivine, orthopyroxene and clinopyroxene at the P–T–X conditions of the final (highest) temperature in each melting interval (that is, before an extraction or phase assemblage change; Supplementary Data 3). Partition coefficients were obtained with online tools available at https://earth-sun.weebly.com/tools.html combining several published models[52–56], on the basis of a wide array of experimental data. Phase-starting proportions were revised for each melting interval (that is, after melt extraction or change in phase assemblage; Supplementary Data 1 and 3).

Fractionation of REEs between solids, residual liquids and extracted liquids was modelled using quantitative incongruent dynamic melting[27]. This allowed non-modal, variable reaction stoichiometry melting and variable-phase $K_D$ to be modelled effectively. Stepwise implementation of the model allowed discontinuous variations of parameters, such as the consumption of a phase or change in bulk composition of the system (for example, cpx-out or melt extractions). Residual melt retention in the trace element model was varied. In one setup, the incremental model retained melt equal to the proportion of residual melt in the major element extractions and 1% melt at phase assemblage change calculations. In a second (end-member) case, the model was rerun with no residual melt.

### Komatiite dataset

For the statistical analysis of Al/Ti systematics of Archaean komatiite, 3,829 published komatiite compositions were extracted from the GEOROC Archaean cratons dataset[57]. Filters were applied to the dataset to limit analyses to minimum age >2.5 Gyr and >18 wt% MgO, and to exclude mantle rocks.

## Data availability

The data that support the findings of this study are available in the paper or its supplementary files (also available on EarthChem https://doi.org/10.26022/ieda/112711), or otherwise available on reasonable request from the corresponding author. Source data are provided with this paper.


41. Powell, R. & Holland, T. An internally consistent dataset with uncertainties and correlations: 3. Applications to geobarometry, worked examples and a computer program. *J. Metamorph. Geol.* **6**, 173–204 (1988).
42. Lexa, O. pypsbuilder, https://pypsbuilder.readthedocs.io/en/latest/index.html (2020).
43. Palin, R. M. et al. High-grade metamorphism and partial melting of basic and intermediate rocks. *J. Metamorph. Geol.* **34**, 871–892 (2016).
44. Kendrick, J. & Yakymchuk, C. Garnet fractionation, progressive melt loss and bulk composition variations in anatectic metabasites: complications for interpreting the geodynamic significance of TTGs. *Geosci. Front.* **11**, 745–763 (2020).
45. Hernández-Montenegro, J. D., Palin, R. M., Zuluaga, C. A. & Hernández-Uribe, D. Archean continental crust formed by magma hybridization and voluminous partial melting. *Sci. Rep.* **11**, 5263 (2021).
46. Takahashi, E. Melting of a dry peridotite KLB-1 up to 14 GPa: implications on the origin of peridotitic upper mantle. *J. Geophys. Res. Solid Earth* **91**, 9367–9382 (1986).
47. Tomlinson, E. L., Kamber, B. S., Hoare, B. C., Stead, C. V. & Ildefonse, B. An exsolution origin for Archean mantle garnet. *Geology* **46**, 123–126 (2018).
48. Jennings, E. S. & Holland, T. J. A simple thermodynamic model for melting of peridotite in the system NCFMASOCr. *J. Petrol.* **56**, 869–892 (2015).
49. Klemme, S. & O'Neill, H. S. The near-solidus transition from garnet lherzolite to spinel lherzolite. *Contrib. Mineral. Petrol.* **138**, 237–248 (2000).
50. McDonough, W. F. & Sun, S.-S. The composition of the Earth. *Chem. Geol.* **120**, 223–253 (1995).
51. Baker, M. B. & Stolper, E. M. Determining the composition of high-pressure mantle melts using diamond aggregates. *Geochim. Cosmochim. Acta* **58**, 2811–2827 (1994).
52. Sun, C. & Liang, Y. Distribution of REE between clinopyroxene and basaltic melt along a mantle adiabat: effects of major element composition, water, and temperature. *Contrib. Mineral. Petrol.* **163**, 807–823 (2012).
53. Sun, C. & Liang, Y. Distribution of REE and HFSE between low-Ca pyroxene and lunar picritic melts around multiple saturation points. *Geochim. Cosmochim. Acta* **119**, 340–358 (2013).
54. Sun, C. & Liang, Y. The importance of crystal chemistry on REE partitioning between mantle minerals (garnet, clinopyroxene, orthopyroxene, and olivine) and basaltic melts. *Chem. Geol.* **358**, 23–36 (2013).
55. Sun, C. & Liang, Y. An assessment of subsolidus re-equilibration on REE distribution among mantle minerals olivine, orthopyroxene, clinopyroxene, and garnet in peridotites. *Chem. Geol.* **372**, 80–91 (2014).
56. Yao, L., Sun, C. & Liang, Y. A parameterized model for REE distribution between low-Ca pyroxene and basaltic melts with applications to REE partitioning in low-Ca pyroxene along a mantle adiabat and during pyroxenite-derived melt and peridotite interaction. *Contrib. Mineral. Petrol.* **164**, 261–280 (2012).
57. Lehnert, K., Su, Y., Langmuir, C. H., Sarbas, B. & Nohl, U. A global geochemical database structure for rocks. *Geochem. Geophys. Geosyst.* **1**, 1012 (2000).
58. Banas, A. et al. Ancient metasomatism recorded by ultra-depleted garnet inclusions in diamonds from DeBeers Pool, South Africa. *Lithos* **112**, 736–746 (2009).
59. Davies, R. M., Griffin, W. L., O'Reilly, S. Y. & Doyle, B. J. Mineral inclusions and geochemical characteristics of microdiamonds from the DO27, A154, A21, A418, DO18, DD17 and Ranch Lake kimberlites at Lac de Gras, Slave Craton, Canada. *Lithos* **77**, 39–55 (2004).
60. Donnelly, C. L., Stachel, T., Creighton, S., Muehlenbachs, K. & Whiteford, S. Diamonds and their mineral inclusions from the A154 South pipe, Diavik Diamond Mine, Northwest territories, Canada. *Lithos* **98**, 160–176 (2007).
61. Harris, J. W., Stachel, T., Léost, I. & Brey, G. P. Peridotitic diamonds from Namibia: constraints on the composition and evolution of their mantle source. *Lithos* **77**, 209–223 (2004).
62. Logvinova, A. M., Taylor, L. A., Floss, C. & Sobolev, N. V. Geochemistry of multiple diamond inclusions of harzburgitic garnets as examined in situ. *Int. Geol. Rev.* **47**, 1223–1233 (2005).
63. Motsamai, T., Harris, J. W., Stachel, T., Pearson, D. G. & Armstrong, J. Mineral inclusions in diamonds from Karowe Mine, Botswana: super-deep sources for super-sized diamonds? *Mineral. Petrol.* **112**, 169–180 (2018).
64. Pokhilenko, N., Sobolev, N., Reutsky, V., Hall, A. & Taylor, L. Crystalline inclusions and C isotope ratios in diamonds from the Snap Lake/King Lake kimberlite dyke system: evidence of ultradeep and enriched lithospheric mantle. *Lithos* **77**, 57–67 (2004).
65. Sobolev, N. V. et al. Mineral inclusions in microdiamonds and macrodiamonds from kimberlites of Yakutia: a comparative study. *Lithos* **77**, 225–242 (2004).
66. Stachel, T. et al. The trace element composition of silicate inclusions in diamonds: a review. *Lithos* **77**, 1–19 (2004).
67. Stachel, T., Brey, G. P. & Harris, J. W. Kankan diamonds (Guinea) I: from the lithosphere down to the transition zone. *Contrib. Mineral. Petrol.* **140**, 1–15 (2000).
68. Stachel, T. & Harris, J. W. Diamond precipitation and mantle metasomatism–evidence from the trace element chemistry of silicate inclusions in diamonds from Akwatia, Ghana. *Contrib. Mineral. Petrol.* **129**, 143–154 (1997).
69. Stachel, T., Viljoen, K., McDade, P. & Harris, J. Diamondiferous lithospheric roots along the western margin of the Kalahari Craton—the peridotitic inclusion suite in diamonds from Orapa and Jwaneng. *Contrib. Mineral. Petrol.* **147**, 32–47 (2004).
70. Tappert, R., Stachel, T., Harris, J. W., Shimizu, N. & Brey, G. P. Mineral inclusions in diamonds from the Panda kimberlite, Slave Province, Canada. *Eur. J. Mineral.* **17**, 423–440 (2005).
71. Tappert, R., Stachel, T., Harris, J. W., Muehlenbachs, K. & Brey, G. P. Placer diamonds from Brazil: indicators of the composition of the earth's mantle and the distance to their kimberlitic sources. *Econ. Geol.* **101**, 453–470 (2006).
72. Viljoen, K., Harris, J., Ivanic, T., Richardson, S. & Gray, K. Trace element chemistry of peridotitic garnets in diamonds from the Premier (Cullinan) and Finsch kimberlites, South Africa: contrasting styles of mantle metasomatism. *Lithos* **208–209**, 1–15 (2014).
73. Wang, W., Sueno, S., Takahashi, E., Yurimoto, H. & Gasparik, T. Enrichment processes at the base of the Archean lithospheric mantle: observations from trace element characteristics of pyropic garnet inclusions in diamonds. *Contrib. Mineral. Petrol.* **139**, 720–733 (2000).
74. Creighton, S. et al. Oxidation of the Kaapvaal lithospheric mantle driven by metasomatism. *Contrib. Mineral. Petrol.* **157**, 491 (2009).
75. Wasch, L. J. et al. An alternative model for silica enrichment in the Kaapvaal subcontinental lithospheric mantle. *Geochim. Cosmochim. Acta* **73**, 6894–6917 (2009).
76. Lazarov, M., Brey, G. P. & Weyer, S. Time steps of depletion and enrichment in the Kaapvaal craton as recorded by subcalcic garnets from Finsch (SA). *Earth Planet. Sci. Lett.* **279**, 1–10 (2009).
77. Lazarov, M., Woodland, A. B. & Brey, G. P. Thermal state and redox conditions of the Kaapvaal mantle: a study of xenoliths from the Finsch mine, South Africa. *Lithos* **112**, 913–923 (2009).
78. Lazarov, M., Brey, G. P. & Weyer, S. Evolution of the South African mantle—a case study of garnet peridotites from the Finsch diamond mine (Kaapvaal craton); Part 2: multiple depletion and re-enrichment processes. *Lithos* **154**, 210–223 (2012).
79. Grégoire, M., Bell, D. & Le Roex, A. Garnet lherzolites from the Kaapvaal Craton (South Africa): trace element evidence for a metasomatic history. *J. Petrol.* **44**, 629–657 (2003).
80. Peslier, A., Woodland, A., Bell, D., Lazarov, M. & Lapen, T. Metasomatic control of water contents in the Kaapvaal cratonic mantle. *Geochim. Cosmochim. Acta* **97**, 213–246 (2012).
81. Schmädicke, E., Gose, J., Reinhardt, J., Will, T. M. & Stalder, R. Garnet in cratonic and non-cratonic mantle and lower crustal xenoliths from southern Africa: composition, water incorporation and geodynamic constraints. *Precambrian Res.* **270**, 285–299 (2015).

82. Shu, Q., Brey, G. P., Gerdes, A. & Hoefer, H. E. Geochronological and geochemical constraints on the formation and evolution of the mantle underneath the Kaapvaal craton: Lu–Hf and Sm–Nd systematics of subcalcic garnets from highly depleted peridotites. *Geochim. Cosmochim. Acta* **113**, 1–20 (2013).
83. Hanger, B. J., Yaxley, G. M., Berry, A. J. & Kamenetsky, V. S. Relationships between oxygen fugacity and metasomatism in the Kaapvaal subcratonic mantle, represented by garnet peridotite xenoliths in the Wesselton kimberlite, South Africa. *Lithos* **212–215**, 443–452 (2015).
84. Hin, R. C. et al. Formation and temporal evolution of the Kalahari sub-cratonic lithospheric mantle: constraints from Venetia xenoliths, South Africa. *Lithos* **112**, 1069–1082 (2009).
85. Boyd, F. et al. Garnet lherzolites from Louwrensia, Namibia: bulk composition and *P*/*T* relations. *Lithos* **77**, 573–592 (2004).
86. Luchs, T., Brey, G., Gerdes, A. & Höfer, H. The lithospheric mantle underneath the Gibeon Kimberlite field (Namibia): a mix of old and young components—evidence from Lu–Hf and Sm–Nd isotope systematics. *Precambrian Res.* **231**, 263–276 (2013).
87. Gibson, S., McMahon, S., Day, J. & Dawson, J. Highly refractory lithospheric mantle beneath the Tanzanian craton: evidence from Lashaine pre-metasomatic garnet-bearing peridotites. *J. Petrol.* **54**, 1503–1546 (2013).
88. Tappert, R., Foden, J., Muehlenbachs, K. & Wills, K. Garnet peridotite xenoliths and xenocrysts from the Monk Hill kimberlite, South Australia: insights into the lithospheric mantle beneath the Adelaide Fold Belt. *J. Petrol.* **52**, 1965–1986 (2011).
89. Creighton, S. et al. Diamondiferous peridotitic microxenoliths from the Diavik Diamond Mine, NT. *Contrib. Mineral. Petrol.* **155**, 541–554 (2008).
90. Creighton, S., Stachel, T., Eichenberg, D. & Luth, R. W. Oxidation state of the lithospheric mantle beneath Diavik diamond mine, central Slave craton, NWT, Canada. *Contrib. Mineral. Petrol.* **159**, 645–657 (2010).
91. Aulbach, S., Griffin, W. L., Pearson, N. J., O'Reilly, S. Y. & Doyle, B. J. Lithosphere formation in the central Slave Craton (Canada): plume subcretion or lithosphere accretion? *Contrib. Mineral. Petrol.* **154**, 409–427 (2007).
92. Aulbach, S., Griffin, W. L., Pearson, N. J. & O'Reilly, S. Y. Nature and timing of metasomatism in the stratified mantle lithosphere beneath the central Slave craton (Canada). *Chem. Geol.* **352**, 153–169 (2013).
93. Klein-BenDavid, O. & Pearson, D. G. Origins of subcalcic garnets and their relation to diamond forming fluids—case studies from Ekati (NWT-Canada) and Murowa (Zimbabwe). *Geochim. Cosmochim. Acta* **73**, 837–855 (2009).
94. Westerlund, K. et al. A subduction wedge origin for Paleoarchean peridotitic diamonds and harzburgites from the Panda kimberlite, Slave craton: evidence from Re–Os isotope systematics. *Contrib. Mineral. Petrol.* **152**, 275–294 (2006).
95. Schmidberger, S. & Francis, D. Constraints on the trace element composition of the Archean mantle root beneath Somerset Island, Arctic Canada. *J. Petrol.* **42**, 1095–1117 (2001).
96. Hunt, L. et al. Small mantle fragments from the Renard kimberlites, Quebec: powerful recorders of mantle lithosphere formation and modification beneath the Eastern Superior Craton. *J. Petrol.* **53**, 1597–1635 (2012).
97. Smit, K., Pearson, D., Stachel, T. & Seller, M. Peridotites from Attawapiskat, Canada: Mesoproterozoic reworking of Palaeoarchaean lithospheric mantle beneath the Northern Superior superterrane. *J. Petrol.* **55**, 1829–1863 (2014).
98. Zheng, J. et al. Mineral chemistry of peridotites from Paleozoic, Mesozoic and Cenozoic lithosphere: constraints on mantle evolution beneath eastern China. *J. Petrol.* **47**, 2233–2256 (2006).
99. Lehtonen, M. L. Analytical geochemistry from "Electron microprobe and LA-ICP-MS analyses of garnet xenocrysts from Kaavi-Kuopio area kimberlites", Version 1.0. Interdisciplinary Earth Data Alliance (IEDA), https://doi.org/10.1594/IEDA/100264 (2013).
100. Lehtonen, M. & O'Brien, H. Mantle transect of the Karelian Craton from margin to core based on PT data from garnet and clinopyroxene xenocrysts in kimberlites. *Bull. Geol. Soc. Finl.* **81**, 79–102 (2009).
101. Lehtonen, M., O'Brien, H., Johanson, B. & Pakkanen, L. Electron microprobe and LA-ICP-MS analyses of mantle xenocrysts from the Arkhangelskaya kimberlite, NW Russia. Geological Survey of Finland, Open File Report M41.2 (2008).
102. Riches, A. J., Liu, Y., Day, J. M., Spetsius, Z. V. & Taylor, L. A. Subducted oceanic crust as diamond hosts revealed by garnets of mantle xenoliths from Nyurbinskaya, Siberia. *Lithos* **120**, 368–378 (2010).
103. Howarth, G. H. et al. Superplume metasomatism: evidence from Siberian mantle xenoliths. *Lithos* **184–187**, 209–224 (2014).
104. Agashev, A. et al. Metasomatism in lithospheric mantle roots: constraints from whole-rock and mineral chemical composition of deformed peridotite xenoliths from kimberlite pipe Udachnaya. *Lithos* **160–161**, 201–215 (2013).
105. Doucet, L. S., Ionov, D. A. & Golovin, A. V. The origin of coarse garnet peridotites in cratonic lithosphere: new data on xenoliths from the Udachnaya kimberlite, central Siberia. *Contrib. Mineral. Petrol.* **165**, 1225–1242 (2013).
106. Ionov, D. A., Doucet, L. S. & Ashchepkov, I. V. Composition of the lithospheric mantle in the Siberian craton: new constraints from fresh peridotites in the Udachnaya-East kimberlite. *J. Petrol.* **51**, 2177–2210 (2010).
107. Pokhilenko, N., Agashev, A., Litasov, K. & Pokhilenko, L. Carbonatite metasomatism of peridotite lithospheric mantle: implications for diamond formation and carbonatite-kimberlite magmatism. *Russ. Geol. Geophys.* **56**, 280–295 (2015).
108. Solov'eva, L., Yasnygina, T. & Egorov, K. Metasomatic parageneses in deep-seated xenoliths from pipes Udachnaya and Komsomol'skaya-Magnitnaya as indicators of fluid transfer through the mantle lithosphere of the Siberian craton. *Russ. Geol. Geophys.* **53**, 1304–1323 (2012).
109. Shchukina, E., Agashev, A., Kostrovitsky, S. & Pokhilenko, N. Metasomatic processes in the lithospheric mantle beneath the V. Grib kimberlite pipe (Arkhangelsk diamondiferous province, Russia). *Russ. Geol. Geophys.* **56**, 1701–1716 (2015).
110. Ziberna, L., Nimis, P., Zanetti, A., Marzoli, A. & Sobolev, N. V. Metasomatic processes in the central Siberian cratonic mantle: evidence from garnet xenocrysts from the Zagadochnaya kimberlite. *J. Petrol.* **54**, 2379–2409 (2013).
111. Sun, S.-S. & McDonough, W. F. Chemical and isotopic systematics of oceanic basalts: implications for mantle composition and processes. *Geol. Soc. Lond. Spec. Publ.* **42**, 313–345 (1989).
112. Salters, V. J. & Longhi, J. Trace element partitioning during the initial stages of melting beneath mid-ocean ridges. *Earth Planet. Sci. Lett.* **166**, 15–30 (1999).

**Acknowledgements** We would like to thank D. Murphy, S. Tappe, C. Gaina and C. Herzberg for discussions on this research topic. Constructive reviews from the journal reviewers (M. Kopylova and anonymous) helped to improve the original manuscript. C.W. thanks O. Lexa for developing and updating pypsbuilder to run the most recent version of THERMOCALC and R. Emo for input on thermodynamic modelling. C.W. acknowledges support from a QUT Postgraduate Research Award.

**Author contributions** C.W. performed all the THERMOCALC and final trace element modelling, drafted most figures, wrote a manuscript outline and prepared the methods, extended data and supplementary data files and revised all of these. B.S.K. wrote most of the paper, edited several iterations and the methods and extended data files, and drafted Fig. 3 and revised the manuscript. E.L.T. conceived the original idea, collated literature data, performed preliminary trace element modelling and edited iterations of the full and revised manuscript. B.S.K. and E.L.T. discussed and advanced the research ideas.

**Competing interests** The authors declare no competing interests.

**Additional information**

**Supplementary information** The online version contains supplementary material available at https://doi.org/10.1038/s41586-022-05665-2.

**Correspondence and requests for materials** should be addressed to Balz S. Kamber.

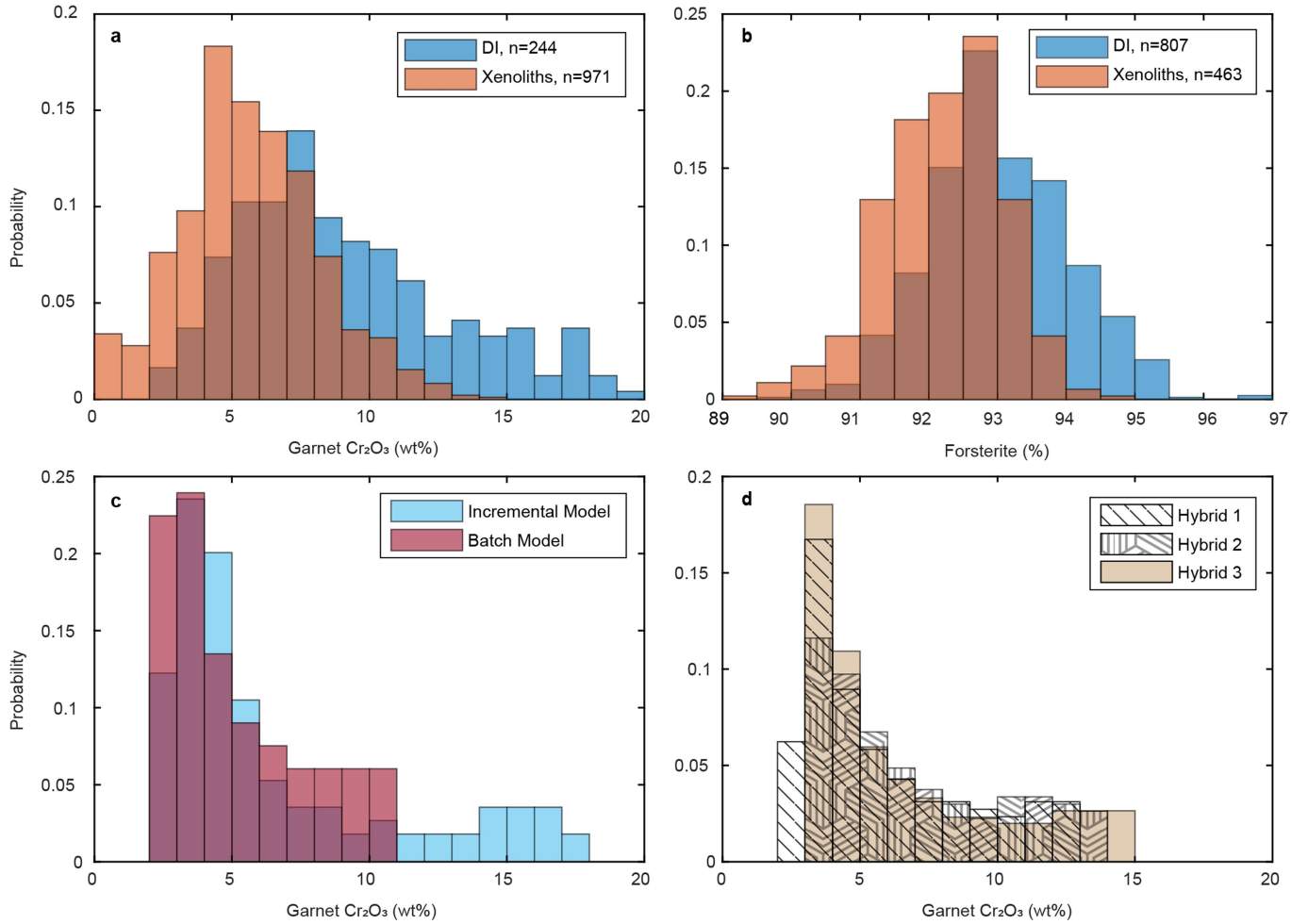


**Extended Data Fig. 1 | Cr in garnet and olivine Fo distribution from compiled literature with model results.** Histograms of: Cr concentrations in global cratonic peridotite garnet and garnet DIs (**a**)[18,37,58–110]; forsterite component in cratonic peridotite olivine and olivine DIs (**b**)[8,24]; garnet $Cr_2O_3$ concentrations in incremental melt model residues and batch KR4003 melt model residues during melting (**c**); garnet $Cr_2O_3$ over the melting interval of hybrid compositions (**d**). Note that DI versus peridotite distinction in **a** and **b** is more pronounced on a craton-by-craton basis than in the global database.

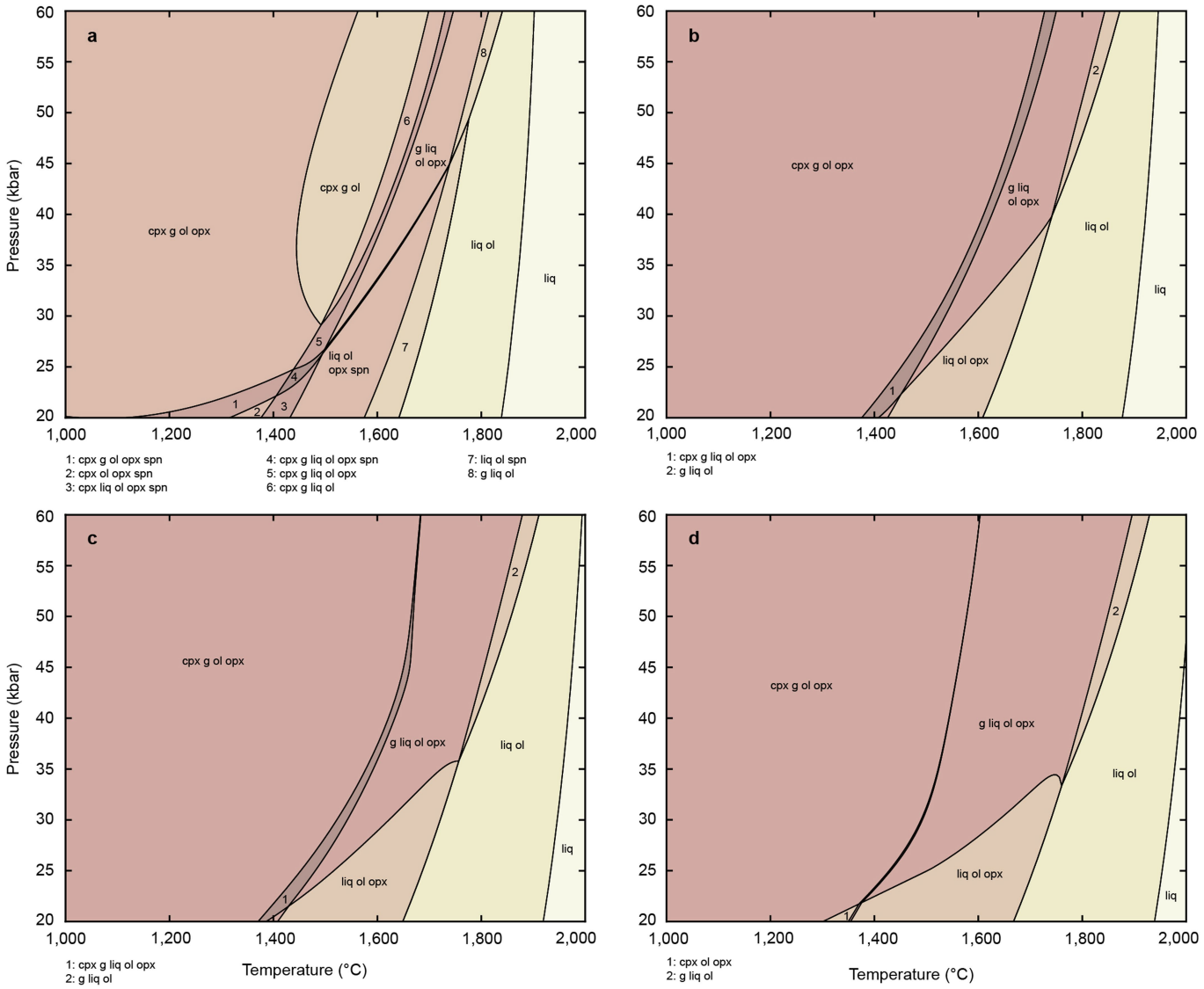


**Extended Data Fig. 2 | THERMOCALC pressure–temperature pseudosections of the four incremental model systems whose chemical compositions are listed in Extended Data Table 1.** Equilibrium phase assemblage is shown for 1,000–2,000 °C, 20–60 kbar for KR4003 (**a**), Ext1 (**b**), Ext2 (**c**) and Ext2.5 (**d**). Each subsequent composition is more refractory than the last, reflected in the increasing simplicity of the phase assemblages and higher liquidus temperatures.

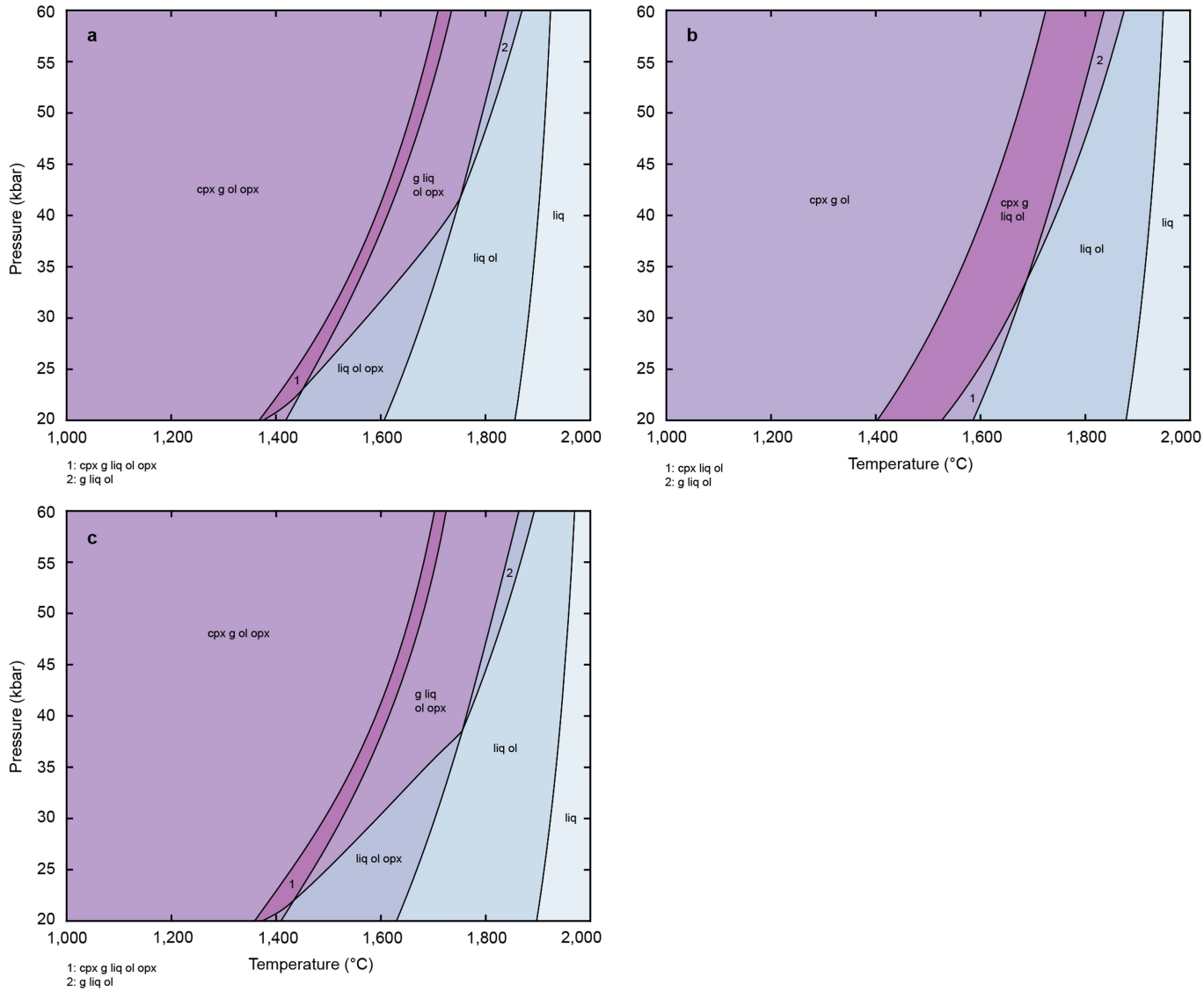


**Extended Data Fig. 3 | THERMOCALC pressure–temperature pseudosections of open-system models.** Hybrids #1 (**a**) and #2 (**b**) are 1:2 mixtures of experimental AUK[22,46] with Ext2 of the incremental model. Hybrid #3 (**c**) uses the more refractory Ext2.5 composition at a 1:4 ratio (see Methods for details). The pyroxene structure stabilized by THERMOCALC is sensitive to compositional 'starting guesses' illustrated in **a** and **b**, in which low-Ca clinopyroxene and high-Ca orthopyroxene have the same composition and are effectively interchangeable.

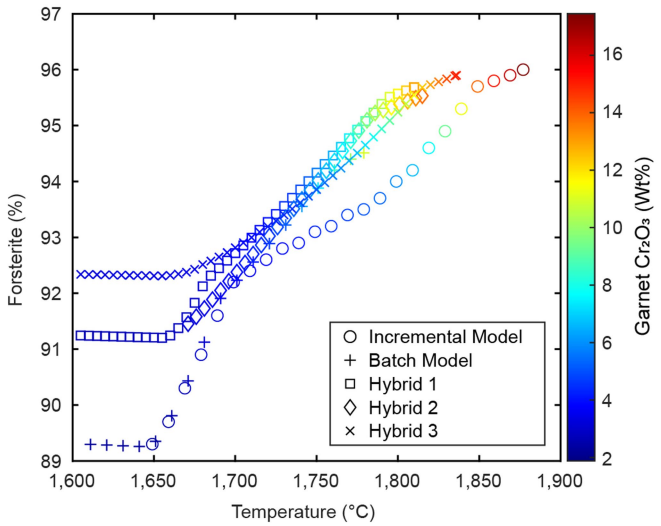


**Extended Data Fig. 4 | Effect of open versus closed systems on forsterite and $Cr_2O_3$ in garnet during advanced melting.** Open-system and batch models show similar evolution in forsterite during progressive melting characterized by a continuous steep increase in forsterite until orthopyroxene is exhausted compared with delayed increase in forsterite component associated with incremental melt extraction. Maximum $Cr_2O_3$ in garnet is <15 wt% in hybrid-system models compared with >17 wt% during incremental melt extraction without komatiite input (incremental model).

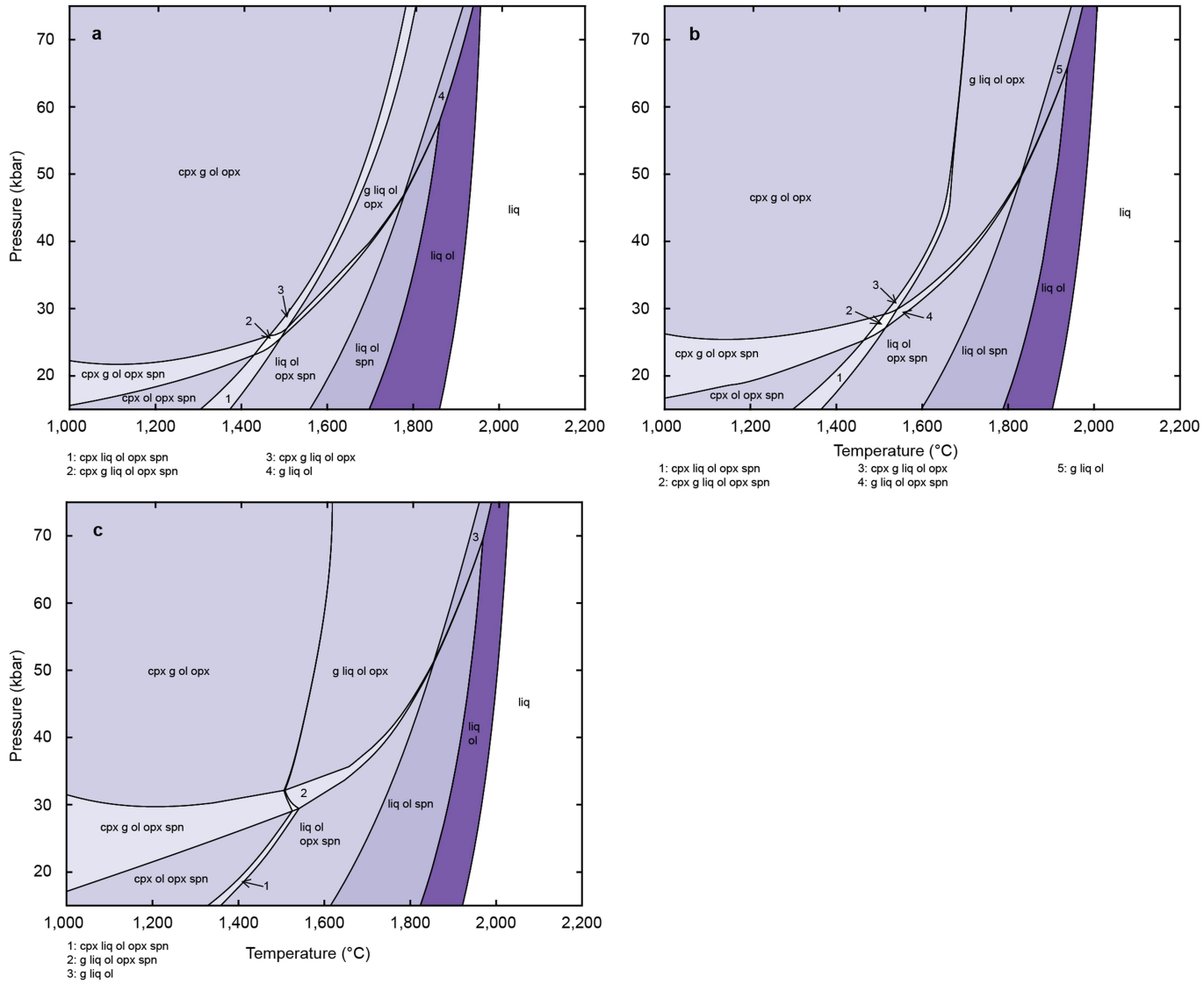


**Extended Data Fig. 5 | THERMOCALC pressure–temperature pseudosections of the incremental model components after KR4003 with spinel enabled. a**, Ext1. **b**, Ext2. **c**, Ext2.5. Progressively more refractory compositions show increased spinel stability up to almost 7 GPa in Ext2.5, albeit at very low modal abundances (<0.007 at 5 GPa). Below 7 GPa, spinel replaces garnet or orthopyroxene as the last phase to coexist with olivine and melt. This unexpected high-pressure-stability spinel is attributed to increased MgO and $Cr_2O_3$ in the residue (over)stabilizing picrochromite in THERMOCALC[21] (see Methods for more details). The effect on $Cr_2O_3$ in garnet is only observed close to garnet exhaustion, in which Cr-rich garnet (<13 wt% $Cr_2O_3$) converts to a spinel structure.

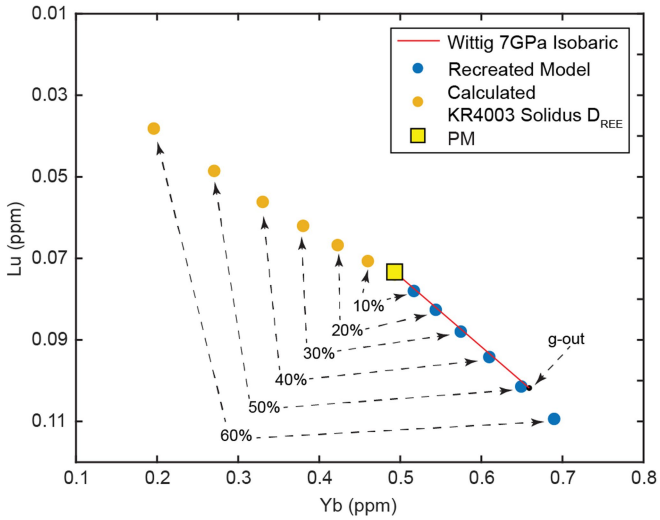


**Extended Data Fig. 6 | Effect of selection of partition coefficients on HREE concentration in modelled residues.** The red line shows the trajectory of the 7-GPa isobaric melt model redrafted from Wittig et al.[7] starting at primitive mantle (PM)[111]. In their model, both Lu and Yb become more enriched with increasing melt fraction until garnet-out (g-out; black dot). We used partition coefficients from references given in Wittig et al.[7] to fit a simple modal batch melting model to their 7-GPa isobaric trajectory. This model used a generic set of partition coefficients for mantle phases to yield bulk partition coefficients of $D_{Yb} = 8.47$ and $D_{Lu} = 9.46$. These result in retention of Lu and Yb in garnet-bearing residues. Individually calculated coefficients for the specific P–T–X conditions (see Methods for details) are considerably lower. They result in an opposite Lu versus Yb trajectory (shown in orange) for an otherwise identical model. Melt fractions are annotated for both models. It is noted that the garnet partition coefficients used in the 7-GPa isobaric model were experimentally derived for a very different tectonic setting—decompression melting beneath a mid-ocean ridge[112].

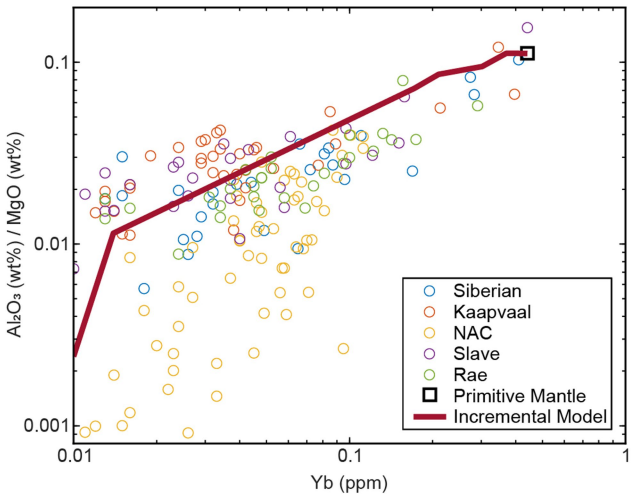


**Extended Data Fig. 7 | Covariation in Al over Mg depletion versus ytterbium depletion.** Whole-rock data for n = 183 cratonic xenoliths from various cratons[7,18,106] (colour-coded as per legend) show a positive correlation between depletion in Al (relative to Mg) and Yb concentration. Superimposed on the observed data is the trend modelled for the restite after isobaric 5-GPa incremental melt loss. This shows the decreasing fertility as the composition trends away from primitive-mantle-like solid composition as gradual consumption of garnet through the series of melting reactions (Fig. 2 inset) reduced Al and increased Mg (see Extended Data Table 1). The gradual consumption of garnet, clinopyroxene and orthopyroxene cause the concomitant decrease in Yb concentration in the restite. The incremental model follows the trend of cratonic xenolith data away from primitive mantle, unlike high-pressure trends suggested in other studies[6].

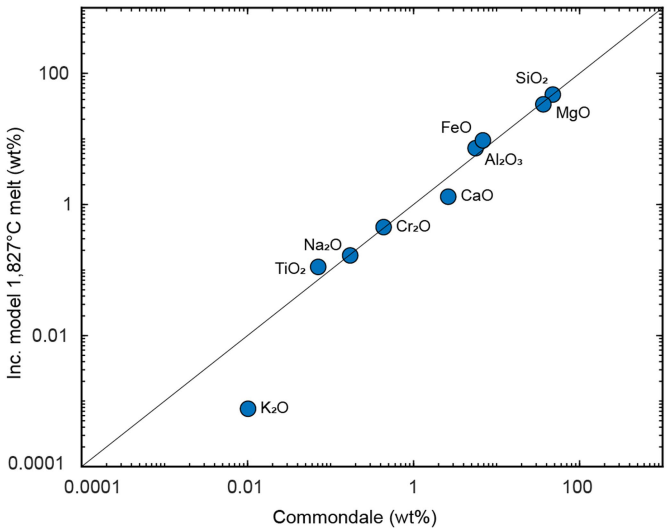


**Extended Data Fig. 8 | Comparison of major element composition of Commondale parental melt with incremental melt model liquid at 5 GPa and 1,827 °C.** There is a generally very strong similarity with oxides plotting above the line slightly enriched in the model (Supplementary Data 1) compared with Commondale komatiite parental melt[12]. Oxides below the theoretical 1:1 line are underestimated in the model.

**Extended Data Table 1 | Major element compositions of experimental starting materials and modelled compositions**

| Bulk Comp | $SiO_2$ (wt%) | $TiO_2$ (wt%) | $Cr_2O_3$ (wt%) | $Al_2O_3$ (wt%) | $Fe_2O_3$ (wt%) | FeO (wt%) | MgO (wt%) | CaO (wt%) | $Na_2O$ (wt%) | $K_2O$ (wt%) |
|---|---|---|---|---|---|---|---|---|---|---|
| Incremental model compositions | | | | | | | | | | |
| KR4003 | 45.44 | 0.17 | 0.41 | 4.31 | 0.18 | 7.96 | 37.74 | 3.49 | 0.23 | 0.09 |
| Ext1 (18%) | 45.16 | 0.13 | 0.47 | 3.91 | 0.10 | 7.10 | 40.85 | 2.09 | 0.18 | 0.02 |
| Ext2 (34%) | 44.79 | 0.06 | 0.52 | 3.24 | 0.06 | 6.30 | 44.15 | 0.79 | 0.09 | 0.00 |
| Ext2.5 (41%) | 44.58 | 0.04 | 0.54 | 2.82 | 0.05 | 5.88 | 45.70 | 0.34 | 0.05 | 0.00 |
| % remaining after Ext2.5 | 98.12 | 21.66 | 132.52 | 65.54 | 27.77 | 73.86 | 121.10 | 9.79 | 22.12 | 0.21 |
| Open system compositions | | | | | | | | | | |
| Run 70.08[22] | 47.46 | 0.28 | 0.50 | 6.47 | 1.44 | 7.33 | 30.37 | 5.63 | 0.41 | 0.11 |
| Run 78[46] | 46.64 | 0.20 | 0.40 | 4.60 | 1.47 | 7.48 | 34.93 | 3.90 | 0.30 | 0.08 |
| Hybrid #1 | 45.66 | 0.13 | 0.48 | 4.32 | 0.50 | 6.66 | 39.54 | 2.40 | 0.19 | 0.04 |
| Hybrid #2 | 45.38 | 0.11 | 0.51 | 3.69 | 0.50 | 6.72 | 41.06 | 1.83 | 0.16 | 0.03 |
| Hybrid #3 | 45.14 | 0.09 | 0.53 | 3.55 | 0.30 | 6.20 | 42.63 | 1.40 | 0.12 | 0.02 |

The pyrolytic KR4003 starting mantle composition[22] is followed by successively more refractory systems after incremental melt extractions. Cumulative melt extraction (wt%) is given in parentheses. Percentage of oxides remaining from KR4003 after Ext2.5 are also listed, highlighting element (in)compatibility. Experimental komatiite liquid compositions[22,46] and open-system komatiite: harzburgite hybrids are given.

## Extended Data Table 2 | Incremental model HREE concentrations at 5 GPa

| | Solidus* | Ext1 | Cpx-out | Ext2 | Ext2.5 | Opx-out | G-out |
|---|---|---|---|---|---|---|---|
| Residue (solid phases + residual melt) | | | | | | | |
| Yb (ppm) | 0.441 | 0.370 | 0.302 | 0.210 | 0.172 | 0.014 | 0.006 |
| Lu (ppm) | 0.068 | 0.059 | 0.050 | 0.037 | 0.031 | 0.003 | 0.001 |
| Extracted Melt | | | | | | | |
| Yb (ppm) | - | 0.811 | 0.836 | 1.105 | 0.615 | 0.402 | 2.061 |
| Lu (ppm) | - | 0.112 | 0.119 | 0.161 | 0.097 | 0.072 | 0.372 |

* PM[51]

For the six melting increments (reflecting change in phase assemblage or system chemistry), new Lu and Yb concentrations were modelled. For residues at extractions (that is, Ext1, Ext2 and Ext2.5), the residual melt was the same as in the THERMOCALC model. For the melting intervals ending at phase-out univariant curves, residual melt was set to 1% of the mass of the system. Across all six melting intervals, $D_{REE}$ for bulk residue is always <1, resulting in melts with Yb and Lu concentrations higher than the starting composition. See Extended Data Table 1 for extent of melting and compositions.